The exceedingly strong two-dimensional ferromagnetism in bi-atomic layer $SrRuO_3$ with a critical conduction transition

Jingxian Zhang[1,§], Long Cheng[2,§], Hui Cao[3,§], Mingrui Bao[2], Jiyin Zhao[4], Xuguang Liu[4], Aidi Zhao[2], Yongseong Choi[5], Hua Zhou[5], Padraic Shafer[6], Xiaofang Zhai[2]

[1]Department of Materials Science and Engineering, University of Science and Technology of China, Hefei 230026, China

[2]School of Physical Science and Technology, ShanghaiTech University, Pudong, Shanghai 201210, China

[3]Materials Science Division, Argonne National Laboratory, Lemont, IL 60439, USA

[4]Instrument Center for Physical Science, University of Science and Technology of China, Hefei 230026, China

[5]X-ray Science Division, Advanced Photon Source, Argonne National Laboratory, Lemont, IL 60439, USA

[6]Advanced Light Source, Lawrence Berkeley National Laboratory, Berkeley, CA 94720, USA

§ Jingxian Zhang, Long Cheng and Hui Cao contributed equally to this work.

ABSTRACT

In recent years, few-layer or even monolayer ferromagnetic materials have drawn a great deal of attention due to the promising integration of two-dimensional (2D) magnets into next-generation spintronic devices. The $SrRuO_3$ monolayer is a rare example of stable 2D magnetism under ambient conditions, but only weak ferromagnetism or antiferromagnetism has been found. The bi-atomic layer $SrRuO_3$ as another environmentally inert 2D magnetic system has been paid less attention heretofore. Here we study both the bi-atomic layer and monolayer $SrRuO_3$ in $(SrRuO_3)_n/(SrTiO_3)_m$ (n=1, 2) superlattices in which the $SrTiO_3$ serves as a non-magnetic and insulating space layer. Although the monolayer exhibits arguably weak ferromagnetism, we find that the bi-atomic layer exhibits exceedingly strong ferromagnetism with a Tc of 125 K and a saturation magnetization of 1.2 μB/Ru, demonstrated by both SQUID magnetometry and element-specific X-ray circular dichroism. Moreover, in the bi-atomic layer $SrRuO_3$, we demonstrate that random fluctuations and orbital reconstructions inevitably occurring in the 2D limit are critical to the electrical transport, but are much less critical to the ferromagnetism. Our study demonstrates that the bi-atomic layer $SrRuO_3$ is an exceedingly strong 2D ferromagnetic oxide which has great potentials for applications of ultracompact spintronic devices.

KEYWORDS

2D ferromagnetism; correlated oxides; $SrRuO_3$; non-Fermi liquid; weak localization

1. Introduction

Since the discovery of the two-dimensional (2D) ferromagnets $Cr_2Ge_2Te_6$ and CrI_3 in 2017 [1, 2], booming interests have been evoked in exploring novel magnetic materials down to few layers or even monolayer. Inspired by the initial work, more 2D magnetic materials have been found and the related research is sprouting up [3, 4]. The reduced dimensionality facilitates the tunability of magnetism by fine external perturbations, making it highly promising for the applications in next-generation spintronic devices [4, 5]. However, most of the experimentally demonstrated 2D ferromagnets are van der Waals materials with poor stability in the ambient environment, and their lateral sizes are small (typically in micrometers) [1-5]. While the correlated transition metal oxides with rich magnetic properties are much more stable and hence great alternative candidates for 2D and size-scalable spintronics applications.

Among the wide variety of correlated transition metal oxides, $SrRuO_3$ (SRO) is a unique example of 4*d* itinerant ferromagnetism (FM) with a transition temperature (Tc) as high as 160 K. It is a Fermi liquid at low temperatures and exhibits strong perpendicular magnetic anisotropy (PMA) under compressive in-plane strain [6-8]. In the past decade, great efforts have been devoted into investigations of ultrathin SRO thin films but the ferromagnetism usually is seriously devastated below a critical thickness of about 4 unit cells [6, 9-12]. The ferromagnetic and metallic state was predicted for the monolayer SRO embedded in the SrTiO3 (STO) matrix [13, 14].

However, the experimental studies gave similar results that the monolayer SRO within the SRO/(STO)m superlattices is only weakly ferromagnetic [15, 16]. Some works even suggested that the intrinsic state of monolayer SRO is antiferromagnetic [17-19]. Despite the lack of the consensus on the intrinsic state of the monolayer SRO, the SRO remains as a top candidate of environmentally inert 2D magnet. Thus, a similar study of the bi-atomic layer SRO only having one more unit cell than the monolayer, would strongly benefit the exploration of 2D ferromagnetism in the SRO system. Furthermore, the sub-nanometer thickness of the bi-atomic layer SRO would have just as much potential as the monolayer for future ultracompact device applications.

Here we fabricate a series of (SRO)n/(STO)m superlattices (n/m SL; n=1, 2 and m=2, 4) and particularly focus on the less-studied bi-atomic layer SRO systems (i.e., 2/m SLs in this work). Both the measurements of superconducting quantum interference device (SQUID) magnetometer and X-ray magnetic circular dichroism (XMCD) confirm the strong ferromagnetism in the bi-atomic layer SRO with a high Tc near 125 K and the prominent saturation magnetization around 1.2 μB/Ru, comparable to the bulk thin film. Besides, the peak splitting of the Ru L3-edge X-ray linear dichroism (XLD) spectra clearly shows that the SRO bi-atomic layer is strongly confined. Moreover, the temperature-dependent resistivity of the 2/m SLs reveals a thermally driven conduction transition from the non-Fermi liquid (NFL) to weakly localized state at a critical temperature T*. This work reveals the strong ferromagnetism in the bi-atomic layer SRO which has been paid less attention before. The robust 2D

ferromagnetism in such a sub-nanometer thick and large-lateral-size film paves the ground for ultracompact spintronic device applications.

2 Experimental details

2.1 Sample fabrication

The (SRO)n/(STO)m superlattices were fabricated by pulsed laser deposition (PLD) assisted with reflective high-energy electron diffraction (RHEED) on the (001) STO single crystalline substrates. Before growth, STO substrates with atomically flat TiO2 layer terminations were obtained via buffered hydrofluoric (BHF) acid etching and subsequent oxygen atmosphere annealing at 960 ℃ for 1 hour. The RHEED system was used to monitor the layer-by-layer growth of the films whose thicknesses were precisely controlled at the single unit cell level. During growth, the temperature of substrate was 670 °C facilitated by an infrared laser heating and the oxygen partial pressure was set at 10 Pa for both the SRO and STO deposition. The pulsed laser frequency and the energy fluence were 2 Hz and 1.8 J/cm^{2,} respectively. After deposition, all samples were cooled down to room temperature with a rate of 25 ℃/min under the same oxygen pressure as that during growth.

2.2 Characterization method

The superlattice periodicity and crystallinity were characterized by X-ray diffraction (XRD) 2θ-ω scans in the 2θ range of 20°–50°. The magnetic properties were probed by a SQUID magnetometer. The transport properties were measured using the four-

probe method. The O K-edge X-ray absorption spectroscopy (XAS) and XMCD measurements were performed on beamline 4.0.2 at the Advanced Light Source (ALS) of Lawrence Berkeley National Laboratory at 10 K under the vacuum of ~ 1×10^{-6} Pa. The Ru L-edge XAS/XLD measurements were conducted on beamline 4-ID-D at the Advanced Photon Source of Argonne National Laboratory at room temperature.

3 Results and discussion

3.1 The coherent epitaxy of the superlattices

The (SRO)n/(STO)m superlattice (n/m SL) is schematically shown in Fig. 1(a), where n and m are the numbers of unit cells (n=1, 2; m=2, 4). The repetition numbers are 20 for 2/m SLs and 40 for 1/m SLs, in order to keep the total thickness of SRO the same. The number of layers is well monitored and controlled by RHEED oscillations during the growth [see Fig. S1]. The XRD 2θ-ω scans of these superlattices show the expected diffraction peaks according to the designed periodicity, as indicated in Fig. 1(b). Fig. 1(c) presents two 2D reciprocal space maps of the 2/2 SL from a 3D map taken around the STO (1 1 2) reflection, which demonstrate that both SRO and STO layers are fully strained with the STO substrate. Atomic Force Microscopy (AFM) measurements are carried out to reveal the surface structure of the superlattice. As shown in Fig. 1(d), the AFM image of the 2/2 SL reveals atomically flat terraces, which confirms the high structural quality of the superlattice.

3.2 Electrical transport properties

Fig. 2 presents the electrical transport results of the SLs. For the SLs with monolayer SRO (named as 1/*m* SL), the resistivity increases monotonically with decreasing temperature, indicating an insulating state (see Fig. 2(a)). In comparison, the SLs with bi-atomic layer SRO (2/*m* SL) undergo a thermally driven conduction transition, which is manifested by the non-monotonical temperature dependence of the resistivity, as shown in Fig. 2(c). Herein, T^* is defined as the critical temperature at the resistivity minimum, which is found to be 123K (130K) for 2/2 SL (2/4 SL). The finding of the metallic nature of the bi-atomic layer SRO is consistent with previous work [9, 12, 19]. However, the almost identical shape of the $\rho(T)$ curve in the 2/2 and 2/4 SLs has not been revealed before, which strongly suggests the tunneling through STO space layer is negligible and both bi-atomic layer are mainly conducting in the 2D plane.

To further elucidate the physics underneath the transport property of each SL, we fit the temperature-dependent resistivity using different models. Fig. 2(b) shows good linear relationships between $\ln(\rho)$ and the $T^{-1/3}$ in the low temperature range (below 65 K) for 1/*m* SLs, in agreement with the 2D variable-range-hopping (VRH) conduction [20, 21]. In the high temperature range (near room temperature) for 1/*m* SLs, the resistivity behavior agrees to the Arrhenius thermal activation model with $\rho(T) \propto \exp(E_a/k_B T)$ [see Fig. S2], where E_a is the thermal activation energy and is ~7 meV for the 1/2 SL and ~32 meV for the 1/4 SL respectively. In contrast, Fig. 2(d) shows the $T^{1/2}$ dependence of the conductivity ($1/\rho$) below T^* for the 2/*m* SLs, in agreement with the weak localization model [22], while the resistivity above T^* can be fitted well with

the equation $\rho(T) = \rho_0 + AT^N$ ($1 \leq N < 2$). The best fittings give the exponent $N = 1.4$ [see Fig. S3] for both the 2/2 and 2/4 SLs indicating the NFL behavior [23, 24]. As predicted by the Landau's phenomenological FL theory for metals [25], the electron-electron scattering cross section varies quadratically with temperature, which dictates the T^2 dependence of the resistivity. However, in the NFL regime, the resistivity usually deviates from the T^2 dependence to T^N ($1 \leq N < 2$) dependence [23, 24]. For SRO, the NFL behavior was proposed to mainly stem from electron-magnon scattering [26] or electron-phonon scattering [27]. We tend to believe that the latter mechanism dominates the transport behavior above T^* in the 2/m SLs, as the ρ-T curves with applied magnetic field of 5 T show negligible variation in the high temperature range [see Fig. S4].

To deepen the insight of the thermally driven NFL to localization crossover in the 2/m SLs, we scale the ρ-T curves into ρ/ρ_{T^*}-T/T^* curves and find that the scaled plots of the 2/2 and 2/4 SLs completely collapse to each other as shown in Fig. 2(e). We extract the ρ-T data of other SRO/STO SLs in literature that exhibit the same critical resistivity upturn [11, 16, 19, 28]. Interestingly, based on the fitting analysis [see Fig. S3], all of them show weak localization below T^* and behave as NFL above T^*. Moreover, the temperature range for best fittings are shown in Fig. 2(f). All samples exhibit similar T_L/T^* (~0.35) and T_H/T^* (~1.4) values, where the T_L denotes the upper temperature bound for the weak localization regime while T_H denotes the lower temperature bound for the NFL regime. Therefore the above analysis indicates that the

conduction transition from NFL to weak localization might be universal in ultrathin SRO close to the 2D limit.

3.3 Magnetization measurements and analysis

Magnetic properties of all the SLs are characterized along the out of plane (OOP) direction with SQUID since the 2/m SLs exhibit a strong PMA. The 1/m SLs exhibit the PMA to eightfold MA transition as m increases [15]. The M-T curves were measured after zero-field-cooling (ZFC) and field-cooling (FC) under a small field of 500 Oe and all the data were recorded during the warming up cycle. In Fig. 3(a) and 3(b), the 1/m SLs show small low-field magnetization (~0.03 μB/Ru at 5 K) with a low Curie temperature (Tc) of ~75 K while the 2/m SLs show much stronger low-field magnetization (~0.4 μB/Ru at 5 K) and an exceedingly high Tc of ~125 K. As far as we know, the Tc of bi-atomic SRO layer herein is among the highest in the related works. To compare the ferromagnetic ordering strength of the 2/m SLs to bulk SRO, the M-T curves of a thick SRO film (60 unit cells) are shown which exhibit a low-field magnetization of ~1 μB/Ru at 5 K and a standard Tc of ~160 K. In addition, Fig. 3(b) reveals the distinct blocking behaviors of bi-atomic SRO layer and bulk SRO as ZFC curves deviate from FC curves below Tc and reach the maxima at the certain (blocking) temperatures.

The magnetic hysteresis loops (M-H) are measured at 5 K for the SLs and the thick SRO film, as shown in Fig. 3(c) and 3(d). The 1/2 SL and 1/4 SL exhibit the similar weak saturation magnetization around 0.6 μB/Ru, while the saturation magnetization

of 2/m SLs reaches 1.2 μB/Ru, similar to that of the SRO thin film. Thus, the magnetization measurements demonstrate the distinctively strong ferromagnetism in bi-atomic layer SRO.

To explore the origin of the strong ferromagnetism in the 2/m SLs, the O K-edge XAS/XMCD measurements on all the SLs and the 60-unit-cell-thick SRO film are carried out. The experimental geometry is depicted in Fig. 4(a). All samples are measured at 10 K with the external magnetic field (H) of 4 T applied normal to the sample surface (H∥[0 0 1]). The XAS spectra are taken with the circularly polarized light with left (σ^+) and right (σ^-) polarizations, and the X-ray incidence is aligned parallel with the magnetic field. The spectra are recorded using the total electron yield (TEY) method. The normalized O K-edge X-ray absorption spectra are shown in Fig. 4(b). The peaks can be assigned to the unoccupied O 2*p* states that hybridize with orbitals of cations [12], such as Ru 4*d* (∼528.9 eV) and Ti 3*d* (∼530.5 eV), as indicated in Fig. 4(b). For the absorption peaks of the hybrid orbitals of Ru 4*d* - O 2*p* (∼528.9 eV) and Ti 3*d* - O 2*p* (∼530.5 eV) (indicated by the dashed lines), no obvious peak shifts between the SLs and the thick SRO thin film are observed. The intensity of the Ru 4*d* - O 2*p* hybridized peak evidently increases with the increasing n or decreasing m in the n/m SLs. Fig. 4(c) shows that a large negative XMCD signal is only observed at ~528.9 eV which corresponds to the Ru 4*d* - O 2*p* hybridized peak, suggesting that the ferromagnetism of the SLs is originating from the Ru 4*d* orbitals. The XMCD signals of the 1/m SLs are hardly visible while that of the 2/m SLs are

unambiguously identified. By the means of XMCD measurements, the distinct ferromagnetism of the 2/m SLs is further confirmed and proved to have its roots in the Ru 4*d* orbitals.

3.4 Quantum confinement induced orbital reconstructions

To further reveal the link between the Ru 4d orbital configurations and the electrical and magnetic properties of SRO SLs, the Ru L_3-edge XAS/XLD spectra are measured using the partial fluorescence yield (PFY) mode by monitoring Ru $L\alpha$ emission at room temperature of n/m SLs. The Ru L_3 absorption edge mainly reflects the electron transition from Ru core $2p_{3/2}$ state to unoccupied 4*d* states, and thus contains direct information of the excited electronic structures of Ru 4d orbitals. Fig. 5(a) shows the polarization dependent XAS spectra of Ru L_3-edge of all the SLs measured with light of out-of-plane polarization ($E_\perp$) and in-plane polarization ($E_\parallel$). After a simple subtraction of the two normalized spectra ($I(E_\parallel) - I(E_\perp)$), we obtain the XLD spectra which clearly show peak splitting in all the SLs, as shown in Fig. 5(b). It implies the Ru 4*d* orbital reconstructions driven by quantum confinement. The absorption of light with $E_\parallel$ polarization is dominated by core level electron transition to d_{xy} and $d_{x^2-y^2}$ orbitals, whereas absorption of light with $E_\perp$ polarization is dominated by transitions to $d_{xz,yz}$ and $d_{3z^2-r^2}$ orbitals. Hence, the two positive peaks in the XLD spectra can be assigned to transitions to d_{xy} and $d_{x^2-y^2}$ orbitals respectively [29, 30]. The energy difference Δ between dxy and $d_{x^2-y^2}$ orbitals is quantitatively extracted from the peak splitting ($\Delta = E(d_{x^2-y^2}) - E(d_{xy})$), as displayed in Fig. 5(c). Limited by the energy resolution, the energy splitting of other orbitals can be hardly obtained. It is found that

Δ of the 2/m SLs are nearly 1 eV smaller than that of the 1/m SLs. Accordingly, the enhanced splitting of Ru 4*d* orbitals in monolayer SRO opens a gap responsible for the insulating nature. In comparison, such a peak splitting Δ was not experimentally observed in thick SRO films [31]. Thus the peak splitting observed in the Ru XLD spectra originates from the confinement effect and the size of Δ indicates the strength of the confinement.

3.5 Discussions

Based on the above XLD results, we give a possible scenario of Ru 4*d* orbital configurations in the SLs in Fig. 5(d). For the bulk SRO, Ru 4d orbital is split into threefold t_{2g} orbitals and twofold e_g orbitals. In the case of the SLs, the t_{2g} and e_g orbitals are further split in varying degrees. In the bulk SRO, the nearly degenerate t_{2g} orbitals are occupied by four electrons. Similarly, in the 2/m SLs, three electrons occupy the spin up channel of the nearly degenerate $d_{xz,yz}$ and d_{xy} orbitals while the fourth one resides in the spin down channel of the slightly lower $d_{xz,yz}$ orbitals as the energy split Δt_{2g} between the d_{xy} orbital and $d_{xz,yz}$ orbitals is not sufficiently large to overwhelm the Hund's coupling. In the 1/m SLs, the degeneracy between d_{xy} and $d_{xz,yz}$ orbitals is further lifted so that Δt_{2g} can compete with the Hund's coupling, resulting in partial spin flip down from the d_{xy} orbital to $d_{xz,yz}$ orbitals. Thus, the 1/m SLs is weakly ferromagnetic while the 2/m SLs is strongly ferromagnetic with comparable saturation magnetization to the thin film. Additionally, the quantum confinement would also narrow the bandwidth of Ru 4*d* subbands which further lift the degeneracy

of the t_{2g} and e_g orbitals [32, 33].

Previously, the pursuit of the thinnest ferromagnetic oxide film has been dwelled on the record thickness of more than 3 unit cells in the SRO/STO superlattices [6, 11, 34] and more than 4 unit cells in the La1-xSrxMnO3/STO superlattices [35, 36]. Here the number of unit cell refers to the magnetic layer thickness. Below such thicknesses, the ferromagnetic order is seriously disrupted. In either cases, the number of 3 or 4 unit cells permits at least one monolayer sitting in the center of a 3D structure. Thus true 2D ferromagnetism has not been revealed. Recently, the magneto-transport studies of bi-atomic layer SRO in SRO/STO superlattices have been done with a focus on possible topological Hall effect [37]. But few studies directly investigated the magnetization except a most recent study by S. Jeong, et al [19]. In their study, they found double ferromagnetic transitions at 75 K and 40 K. In the latter transition, the resistivity upturn is also accompanied. Therefore our bi-atomic layer SRO has the exceedingly high transition temperature of 125 K and the highest saturation magnetization of 1.2 μB/Ru, in the family of correlated magnetic oxides in the 2D limit.

4 Conclusion

In conclusion, we have successfully grown high quality (SRO)n/(STO)m superlattices with monolayer and bi-atomic layer SRO, and systematically studied the electrical and magnetic properties as well as the orbital configurations. The monolayer SRO is

weakly ferromagnetic and insulating, while the bi-atomic layer SRO is conducting with an exceedingly strong ferromagnetic order (T_c ~ 125 K and saturation magnetization ~1.2 μB/Ru). Strikingly, both bi-atomic layer SRO undergo identical thermally driven transition from NFL to weak localization. The drastically different electrical and magnetic properties are found to be closely related to the orbital reconstructions driven by quantum confinement, which emerges in both the monolayer and bi-atomic layer SRO but with different strength (~1 eV difference in orbital splitting). Our study presents the exceedingly strong 2D ferromagnetism in correlated oxide thin films and superlattices. It also offers a comprehensive understanding of the fundamental properties of bi-atomic layer SRO different from the monolayer or other ultrathin SRO films. The finding reveals great potentials of fabricating high-quality 2D correlated oxide thin films for future spintronic applications.

Acknowledgements

The work was supported by the National Science Foundation of China (No. 52072244, No. 12104305), the Science and Technology Commission of Shanghai Municipality (No. 21JC1405000) and the ShanghaiTech Startup Fund. This research used resources of the Advanced Photon Source, a U.S. Department of Energy (DOE) Office of Science User Facility operated for the DOE Office of Science by Argonne National Laboratory under Contract No. DE-AC02-06CH11357 and the Advanced Light Source, a U.S. DOE Office of Science User Facility under Contract No. DE-AC02-05CH11231.

References

[1] Gong, C.; Li, L.; Li, Z. L.; Ji, H. W.; Stern, A.; Xia, Y.; Cao, T.; Bao, W.; Wang, C. Z.; Wang, Y. A.; Qiu, Z. Q.; Cava, R. J.; Louie, S. G.; Xia, J.; Zhang, X. Discovery of intrinsic ferromagnetism in two-dimensional van der waals crystals. Nature 2017, 546, 265-269.

[2] Huang, B.; Clark, G.; Navarro-Moratalla, E.; Klein, D. R.; Cheng, R.; Seyler, K. L.; Zhong, D.; Schmidgall, E.; McGuire, M. A.; Cobden, D. H.; Yao, W.; Xiao, D.; Jarillo-Herrero, P.; Xu, X. D. Layer-dependent ferromagnetism in a van der waals crystal down to the monolayer limit. Nature 2017, 546, 270-273.

[3] Gong, C.; Zhang, X. Two-dimensional magnetic crystals and emergent heterostructure devices. Science 2019, 363, eaav4450.

[4] Zhang, S. Q.; Xu, R. Z.; Luo, N. N.; Zou, X. L. Two-dimensional magnetic materials: structures, properties and external controls. Nanoscale 2021, 13, 1398-1424.

[5] Liu, Z.; Deng, L. J.; Peng, B. Ferromagnetic and ferroelectric two-dimensional materials for memory application. Nano Res. 2021, 14, 1802-1813.

[6] Klein, L.; Dodge, J. S.; Ahn, C. H.; Snyder, G. J.; Geballe, T. H.; Beasley, M. R.;

Kapitulnik, A. Anomalous spin scattering effects in the badly metallic itinerant ferromagnet SrRuO3. Phys. Rev. Lett. 1996, 77, 2774-2777.

[7] Xia, J.; Siemons, W.; Koster, G.; Beasley, M. R.; Kapitulnik, A. Critical thickness for itinerant ferromagnetism in ultrathin films of SrRuO3. Phys. Rev. B 2009, 79, 140407.

[8] Klein, L.; Dodge, J. S.; Geballe, T. H.; Kapitulnik, A.; Marshall, A. F.; Antognazza, L.; Char, K. Perpendicular magnetic-anisotropy and strong magnetooptic properties of SrRuO3 epitaxial-films. Appl. Phys. Lett. 1995, 66, 2427-2429.

[9] Izumi, M.; Nakazawa, K.; Bando, Y. T-c suppression of SrRuO3/SrTiO3 superlattices. J. Phys. Soc. Jpn. 1998, 67, 651-654.

[10] Liu, Z. Q.; Ming, Y.; Lu, W. M.; Huang, Z.; Wang, X.; Zhang, B. M.; Li, C. J.; Gopinadhan, K.; Zeng, S. W.; Annadi, A.; Feng, Y. P.; Venkatesan, T.; Ariando. Tailoring the electronic properties of SrRuO3 films in SrRuO3/LaAlO3 superlattices. Appl. Phys. Lett. 2012, 101, 223105.

[11] Bern, F.; Ziese, M.; Setzer, A.; Pippel, E.; Hesse, D.; Vrejoiu, I. Structural, magnetic and electrical properties of SrRuO3 films and SrRuO3/SrTiO3 superlattices. J. Phys. Condens. Matter 2013, 25, 496003.

[12] Jeong, H.; Jeong, S. G.; Mohamed, A. Y.; Lee, M.; Noh, W. S.; Kim, Y.; Bae, J. S.; Choi, W. S.; Cho, D.Y. Thickness-dependent orbital hybridization in ultrathin SrRuO3 epitaxial films. Appl. Phys. Lett. 2019, 115, 092906.

[13] Verissimo-Alves, M.; García-Fernández, P.; Bilc, D. I.; Ghosez, P.; Junquera, J. Highly confined spin-polarized two-dimensional electron gas in SrTiO3/SrRuO3

superlattices. Phys. Rev. Lett. 2012, 108, 107003.

[14] Huang, A.; Hung, S.H.; Jeng, H.T. Strain induced metal–insulator transition of magnetic SrRuO3 single layer in SrRuO3/SrTiO3 superlattice. Appl. Sci. 2018, 8, 2151.

[15] Cui, Z. Z.; Grutter, A. J.; Zhou, H.; Cao, H.; Dong, Y. Q.; Gilbert, D. A.; Wang, J. Y.; Liu, Y. S.; Ma, J. J.; Hu, Z. P.; Guo, J. H.; Xia, J.; Kirby, B. J.; Shafer, P.; Arenholz, E.; Chen, H. H.; Zhai, X. F.; Lu, Y. L. Correlation-driven eightfold magnetic anisotropy in a two-dimensional oxide monolayer. Sci. Adv. 2020, 6, eaay0114.

[16] Boschker, H.; Harada, T.; Asaba, T.; Ashoori, R.; Boris, A. V.; Hilgenkamp, H.; Hughes, C. R.; Holtz, M. E.; Li, L.; Muller, D. A.; Nair, H.; Reith, P.; Wang, X. R.; Schlom, D. G.; Soukiassian, A.; Mannhart, J. Ferromagnetism and conductivity in atomically thin SrRuO3. Phys. Rev. X 2019, 9, 011027.

[17] Mahadevan, P.; Aryasetiawan, F.; Janotti, A.; Sasaki, T. Evolution of the electronic structure of a ferromagnetic metal: Case of SrRuO3. Phys. Rev. B 2009, 80, 035106.

[18] Si, L.; Zhong, Z. C.; Tomczak, J. M.; Held, K. Route to room-temperature ferromagnetic ultrathin SrRuO3 films. Phys. Rev. B 2015, 92, 041108.

[19] Jeong, S. G.; Min, T.; Woo, S.; Kim, J.; Zhang, Y. Q.; Cho, S. W.; Son, J.; Kim, Y. M.; Han, J. H.; Park, S.; Jeong, H. Y.; Ohta, H.; Lee, S.; Noh, T. W.; Lee, J.; Choi, W. S. Phase instability amid dimensional crossover in artificial oxide crystal. Phys. Rev. Lett. 2020, 124, 026401.

[20] Xie, X. C.; Dassarma, S. Transition from one-dimensional to two-dimensional fluctuating variable-range-hopping conduction in microstructures. Phys. Rev. B 1987, 36, 4566-4569.

[21] Tsigankov, D. N.; Efros, A. L. Variable range hopping in two-dimensional systems of interacting electrons. Phys. Rev. Lett. 2002, 88, 176602.

[22] Lee, P. A.; Ramakrishnan, T. V. Disordered electronic systems. Rev. Mod. Phys. 1985, 57, 287-337.

[23] Stewart, G. R. Non-Fermi-liquid behavior in d- and f-electron metals. Rev. Mod. Phys. 2001, 73, 797-855.

[24] Miranda, E.; Dobrosavljević, V. Disorder-driven non-Fermi liquid behaviour of correlated electrons. Rep. Prog. Phys. 2005, 68, 2337-2408.

[25] Altshuler, B. L.; Aronov, A.G. Fermi-liquid theory of the electron-electron interaction effects in disordered metals. Solid State Commun 1983, 46, 429-435.

[26] Dwivedi, G. D.; Sun, S. J.; Kuo, Y. K.; Chou, H. Role of electron-magnon interaction in non-Fermi liquid behavior of SrRuO3. J. Phys. Condens. Matter 2019, 31, 125602.

[27] Allen, P. B.; Berger, H.; Chauvet, O.; Forro, L.; Jarlborg, T.; Junod, A.; Revaz, B.; Santi, G. Transport properties, thermodynamic properties, and electronic structure of SrRuO3. Phys. Rev. B 1996, 53, 4393-4398.

[28] Meng, M.; Wang, Z.; Fathima, A.; Ghosh, S.; Saghayezhian, M.; Taylor, J.; Jin, R. Y.; Zhu, Y. M.; Pantelides, S. T.; Zhang, J. D.; Plummer, E. W.; Guo, H. W. Interface-induced magnetic polar metal phase in complex oxides. Nat. Commun. 2019, 10,

5248.

[29] Jeong, S. G.; Han, G.; Song, S.; Min, T.; Mohamed, A. Y.; Park, S.; Lee, J.; Jeong, H. Y.; Kim, Y. M.; Cho, D. Y.; Choi, W. S. Propagation control of octahedral tilt in SrRuO3 via artificial heterostructuring. Adv. Sci. 2020, 7, 2001643.

[30] Lee, H. G.; Wang, L. F.; Si, L.; He, X. Y.; Porter, D. G.; Kim, J. R.; Ko, E. K.; Kim, J.; Park, S. M.; Kim, B.; Wee, A. T. S.; Bombardi, A.; Zhong, Z. C.; Noh, T. W. Atomic-scale metal-insulator transition in SrRuO3 ultrathin films triggered by surface termination conversion. Adv. Mater. 2020, 32, 1905815.

[31] Agrestini, S.; Hu, Z.; Kuo, C. Y.; Haverkort, M. W.; Ko, K. T.; Hollmann, N.; Liu, Q.; Pellegrin, E.; Valvidares, M.; Herrero-Martin, J.; Gargiani, P.; Gegenwart, P.; Schneider, M.; Esser, S.; Tanaka, A.; Komarek, A. C.; Tjeng, L. H. Electronic and spin states of SrRuO3 thin films: An x-ray magnetic circular dichroism study. Phys. Rev. B 2015, 91, 075127.

[32] Chang, Y. J.; Kim, C. H.; Phark, S. H.; Kim, Y. S.; Yu, J.; Noh, T. W. Fundamental thickness limit of itinerant ferromagnetic SrRuO3 thin films. Phys. Rev. Lett. 2009, 103, 057201.

[33] Kang, S.; Tseng, Y.; Kim, B. H.; Yun, S.; Sohn, B.; Kim, B.; McNally, D.; Paris, E.; Kim, C. H.; Kim, C.; Noh, T. W.; Ishihara, S.; Schmitt, T.; Park, J. G. Orbital-selective confinement effect of Ru 4d orbitals in SrRuO3 ultrathin film. Phys. Rev. B 2019, 99, 045113.

[34] Toyota, D.; Ohkubo, I.; Kumigashira, H.; Oshima, M.; Ohnishi, T.; Lippmaa, M.; Kawasaki, M.; Koinuma, H. Ferromagnetism stabilization of ultrathin SrRuO3 films:

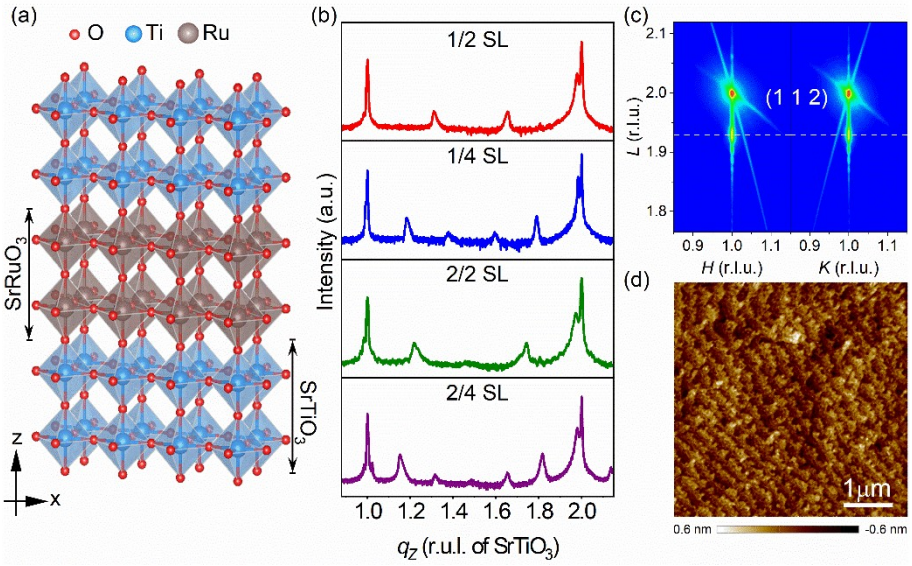

Thickness-dependent physical properties. J. Appl. Phys. 2006, 99, 08N505.

[35] Kourkoutis, L. F.; Song, J. H.; Hwang, H. Y.; Muller, D. A. Microscopic origins for stabilizing room-temperature ferromagnetism in ultrathin manganite layers. Proc. Natl. Acad. Sci. U.S.A. 2010, 107, 11682-11685.

[36] Liao, Z. L.; Li, F. M.; Gao, P.; Li, L.; Guo, J. D.; Pan, X. Q.; Jin, R.; Plummer, E. W.; Zhang, J. D. Origin of the metal-insulator transition in ultrathin films of La2/3Sr1/3MnO3. Phys. Rev. B 2015, 92, 125123.

[37] Wu, P. C.; Song, H. L.; Yuan, Y.; Feng, B.; Ikuhara, Y.; Huang, R.; Yu, P.; Duan, C. G.; Chu, Y. H. Thickness dependence of transport behaviors in SrRuO3/SrTiO3 superlattices. Phys. Rev. Mater. 2020, 4, 014401.

Figure 1 Structural characterizations of $(SRO)_n/(STO)_m$ superlattices. (a) Schematic of the 2/2 SL. (b) XRD 2θ-ω scans of *n*/*m* SLs of (0 0 *L*). (c) X-ray diffraction (XRD) reciprocal space maps of the 2/2 SL taken around the (1 1 2) reflections of the STO substrate. (d) The atomic force microscopy image (5 μm × 5 μm) of the 2/2 SL. The white scale bar represents 1μm.

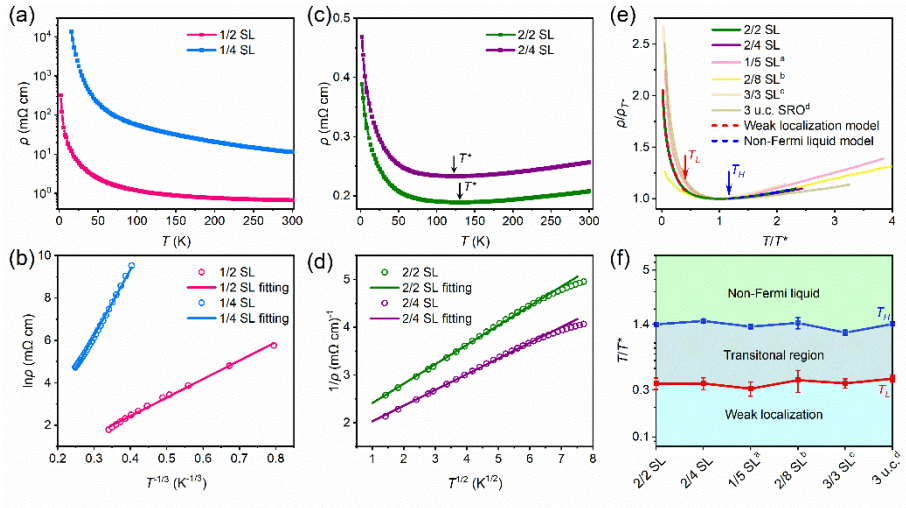

Figure 2 Electrical transport behaviors of $(SRO)_n/(STO)_m$ superlattices. (a) Temperature dependence of the resistivity ρ for 1/m SLs. (b) ln(ρ) vs $T^{-1/3}$ for 1/m SLs below 65 K. (c) Temperature dependence of the resistivity ρ for 2/m SLs. The arrow marks the critical temperature (T*) at which the resistivity reaches its minimum. (d) 1/ρ vs $T^{1/2}$ for 2/m SLs below 60 K. (e) The scaled plots ρ/ρ_{T^*} vs T/T^* for 2/m SLs in this work and others from the literatures. All the data can be fitted well with the weak localization model below T^* and the non-Fermi liquid model above T^*, T_L (T_H) denotes the upper (lower) bound for best fitting in the low (high) temperature range. The 1/5 SL[a], 2/8 SL[b], 3/3 SL[c] and 3 unit-cell (u.c.) SRO[d] are from Ref. [11], [16], [19] and [28], respectively. (f) The universal phase diagram with identical T/T^* dependence.

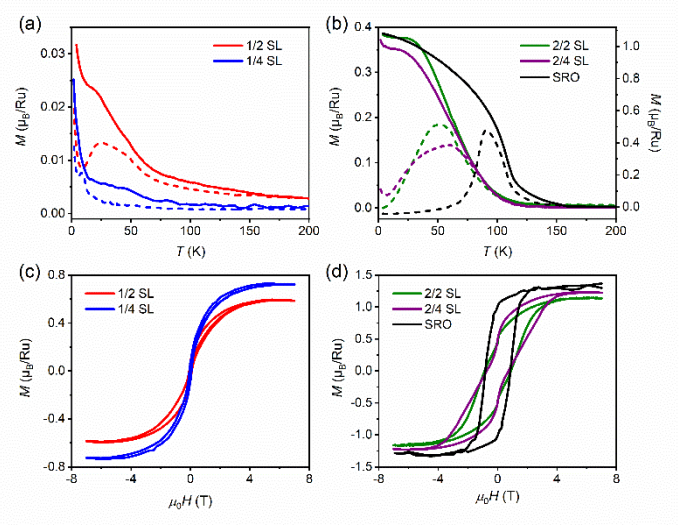

Figure 3 Magnetization characterizations of $(SRO)_n/(STO)_m$ superlattices. Temperature dependence of the magnetization measured under an out-of-plane magnetic field of 500 Oe for (a) 1/*m* SLs and (b) 2/*m* SLs and thick SRO film (60 unit cells) as the bulk counterpart. The solid (dashed) lines represent *M*-*T* curves under field cooling (zero field cooling) conditions. Out-of-plane hysteresis loops at 5 K for (c) 1/*m* SLs and (d) 2/*m* SLs and bulk SRO.

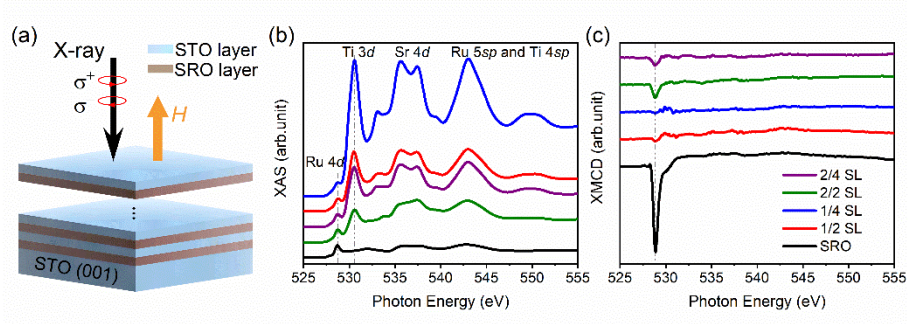

Figure 4 O *K*-edge XAS/XMCD characterizations of $(SRO)_n/(STO)_m$ superlattices at 10 K under the magnetic field of 4 T (H∥[0 0 1]). (a) The experimental geometry. (b) O *K*-edge XAS spectra of *n*/*m* SLs and bulk SRO. The dashed lines indicate the absorption peaks of Ru 4*d* - O 2*p* (∼528.9 eV) and Ti 3*d* - O 2*p* (∼530.5 eV). (c) O *K*-edge XMCD spectra of *n*/*m* SLs and bulk SRO. The dashed line indicates the absorption peak of Ru 4*d* - O 2*p* (∼528.9 eV).

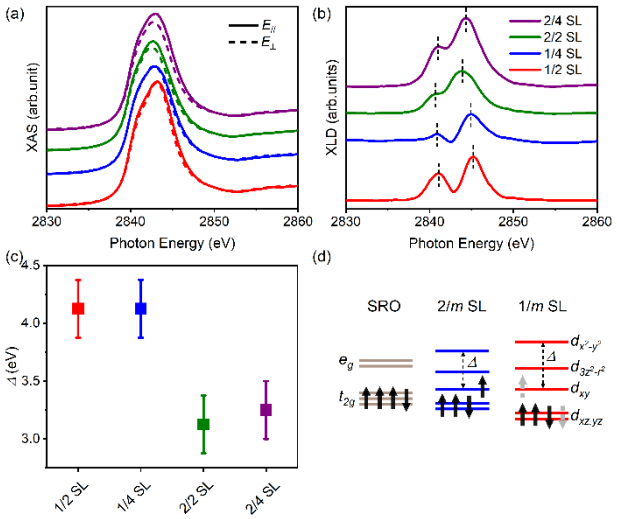

Figure 5 Ru L_3-edge XAS/XLD characterizations of $(SRO)_n/(STO)_m$ superlattices at room temperature. (a) The polarization dependent XAS spectra of Ru L_3-edge of *n*/*m* SLs. (b) The Ru L_3-edge XLD spectra of *n*/*m* SLs. The dashed lines label the positions of the energy split peaks. (c) The energy splitting $\Delta = E(d_{x^2-y^2}) - E(d_{xy})$ of *n*/*m* SLs. (d) A possible scenario of Ru 4*d* orbital configurations for bulk SRO, 2/*m* SLs and 1/*m* SLs under different confinements. Black solid (grey dashed) arrows represent fully (partially) occupied spin states.